CrystEngComm

PAPER

View Article Online
View Journal | View Issue

Cite this: *CrystEngComm*, 2022, **24**, 3701

Exploring the influence of polymorphism and chromophore co-ligands on linkage isomer photoswitching in [Pd(bpy4dca)(NO$_2$)$_2$]†‡

Ben A. Coulson and Lauren E. Hatcher *

Received 15th February 2022,
Accepted 25th March 2022

DOI: 10.1039/d2ce00213b

rsc.li/crystengcomm

The polymorphic Pd(II)–nitrite complex [Pd(bpy4dca)(NO$_2$)$_2$] (**1**) (bpy4dca = 2,2′-bipyridine-4,4′-dicarboxylic acid methyl ester) is shown to undergo photoinduced nitro → nitrito linkage isomer switching in two crystal forms, to varying excited state population levels. Detailed photocrystallographic kinetic studies, structural analyses of the ground and photoexcited states and density functional theory calculations all combine to explain the unusually high maximum excited state population of 80% in **1**, where other linkage isomer complexes containing strong chromophore co-ligands have traditionally been challenging to excite. Comparison of the photo-response in crystals for forms I and II reveals that, while the local crystal packing environment has a role in controlling the maximum photostationary population that can be achieved, the rate of isomerisation is comparable across different nitrite ligand environments. Our results reinforce the hypothesis that a complex combination of steric, electronic and kinetic factors govern the progress of linkage isomer switching in the solid-state and highlight the need for better understanding of the structural dynamics involved in isomer switching at the molecular level.

Introduction

Photoswitches are materials containing some fragment that can undergo a structural change in response to light irradiation. Typically, they can exist in one of two (meta) stable, structurally-distinct states, A and B, that are in equilibrium such that, while A → B switching occurs photochemically, B → A back-conversion is thermally-activated. A wide variety of organic,[1–3] inorganic,[4–6] and organometallic[7–10] photoswitchable molecules are known and are well-studied for applications including optoelectronics, photocatalysis, data storage and solar energy.[11–16]

For many real-world applications, it is convenient to have materials that can switch in the solid state. To fully-analyse structure changes in solid media, it is also desirable to study them by *in situ* single-crystal X-ray diffraction (SCXRD) as this provides highly-accurate, 3D structure information at stages of the photoreaction. For these "photocrystallography" studies, we additionally require that switching occurs in a single-crystal-to-single-crystal manner. This can be challenging, particularly where switching requires a large structural rearrangement. Steric hinderance due to the close packing of molecules in the crystalline state often results in incomplete photoactivation and may even preclude switching altogether, resulting in a complete loss of functionality. Where molecules cannot be switched in the "neat" single-crystal, approaches to dilute the photoactive species in a solid matrix have been explored, *e.g.* incorporation into porous solids such as silica-based materials,[17] metal organic frameworks,[18–20] or other supramolecular solids.[21–24] While many such approaches are successful in providing the necessary space for solid state switching to proceed, the introduction of a complex framework structure can make analysis challenging. This is particularly true for photocrystallographic studies, as framework materials often produce only weakly diffracting crystals. The low resolution diffraction data make it difficult to obtain atomic-scale 3D structure solutions, which are critical to understand the target molecular switching process in detail.

An alternative approach is to rationally design molecular photoswitches whose crystal structure can accommodate the required rearrangements. This route is based on the "reaction cavity" concept, originally proposed by Cohen[25] and later championed by Ohashi *et al.*[26,27] Here, we define a reaction cavity as the region surrounding the photoactive part of the system, such that all necessary atomic rearrangements will occur within the cavity volume. It is then possible to

School of Chemistry, Cardiff University, Main Building, Park Pl, Cardiff CF10 3AT, UK. E-mail: HatcherL1@cardiff.ac.uk

† Dedicated to Paul R. Raithby, celebrating a career in inorganic and organometallic chemistry, on the occasion of his 70th birthday.

‡ Electronic supplementary information (ESI) available. CCDC 2151937 (bpy4dca), 2151942–2151945 (polymorph I) and 2151954–2151981 (polymorph II) contain the crystallographic data for this paper. For ESI and crystallographic data in CIF or other electronic format see DOI: **https://doi.org/10.1039/d2ce00213b**

design the surrounding crystalline environment in a way that maximises the reaction cavity space, for example by choosing ancillary fragments with high steric demands (*e.g.* bulky counterions, co-ligands or co-formers). These bulky, photoinert fragments can then dominate the crystal packing and will remain unchanged on illumination, allowing photoswitching to proceed to high completeness within the reaction cavity volume.

A group of photoswitches that are well-studied in reference to these design principles are solid-state linkage isomers. These switchable organometallics contain ambidentate ligands whose coordination geometry can be switched by exposing the crystal to external stimuli such as light or heat.[28] Photoinduced linkage isomers exist as long-lived metastable states in the crystal, with excited state (ES) lifetimes that are temperature dependent.[29] A variety of linkage isomers have been studied, including nitrosyl, sulfur dioxide, dinitrogen and nitrite complexes.[30–36] While the structure changes involved in photoswitching are relatively modest, involving movement of only a few atoms, early studies were nevertheless hampered by relatively low ES populations in the single-crystal. This changed following a seminal study by Raithby, Warren *et al.* in 2009, in which complete, 100% photoswitching was achieved in single-crystals of the nickel–nitrite complex [Ni(dppe)(NO_2)Cl] (dppe = 1,2-bis(diphenylphosphino)ethane).[35] This study led to a dedicated approach by us,[37–39] and others,[40,41] in designing linkage isomer crystals by considering the steric demands of ancillary groups. This has been particularly successful for group 10 metal-nitrite systems, with 6 materials reported to achieve 100%, reversible nitro → nitrito photoswitching in the single-crystal.[35,37–39,42]

It is notable that all of the nitrite complexes that undergo high ES photoconversion contain ancillary fragments and/or co-ligands that are not, in themselves, strong chromophores. In particular, the most successful complexes contain co-ligands that have aliphatic backbones, *e.g.* 1,2-bis(phosphino)ethane or ethylenediamine derivatives. Anecdotal evidence from our research over the last 10 years indicates that compounds having co-ligands with extended pi-systems (bipyridine, biquinoline, phenanthroline *etc.*) led to crystals with lower,[43] or even no photoswitching capability under the typical conditions used by us to study linkage isomers of this type (*e.g.* T = 100–150 K, λ = 390–450 nm). This is unfortunate, given the wide range of molecular design space that is excluded by this limitation.

Despite the obvious influence of steric factors on solid state photoswitching, the above observations reinforce the fact that the electronic structure of the molecular photoswitch must also impact the achievable ES population level in the crystal.[44] Prior work has shown it can be difficult to deconvolute the impact of steric and electronic effects on the solid state photoreaction; ideally to study these influences separately we require crystal systems that contain identical photoswitchable molecules in differing crystal environments. This has been achieved in a handful of molecular crystal systems where $Z' > 1$, which have more than one crystallographically independent photoswitch in the asymmetric unit.[45,46] However, in these crystals it is difficult to be certain that photoswitching in one molecule does not adversely influence the environment at the second, *i.e. via* the creation of additional steric strain on molecule #2 as a result of switching in molecule #1. Another option would be to study photoswitching in two different polymorphs of the same complex. Theoretically, as both crystals contain chemically identical species, the effect of the different crystal packing environments on switching can be more systematically studied. However, the availability of suitable polymorphic systems for systematic study is, unsurprisingly, low.

Thus, to better understand all of the above factors, we initiated a systematic investigation of linkage isomer systems containing planar aromatic co-ligands, paying particular attention for the propensity for polymorphism. As part of this programme, we here-in report the design, synthesis and photocrystallographic study of two different polymorphs of the simple aromatic linkage isomer complex **1**: [Pd(bpy4dca)(NO_2)$_2$] (bpy4dca = 2,2′-bipyridine-4,4′-dicarboxylic acid methyl ester), and attempt to rationalise its photoswitching behaviour in terms of steric, electronic and kinetic control factors.

Experimental

Synthetic procedures

All manipulations were carried out in air. Palladium(II) acetate, bpy4dca were purchased from Merck Life Science. Potassium nitrite was purchased from Acros Organics. All reagents were used as received without the need for further purification.

Potassium tetranitropalladate was prepared by the reaction of palladium(II) acetate and potassium nitrite, as previously described.[38] bpy4dca was prepared by Fischer esterification following a literature procedure.[47] The crystal structure of bpy4dca is not previously reported in the CSD, and was obtained from a single-crystal grown by slow evaporation of the powder product from chloroform (see ESI‡ §1 for further information).

Preparation of complex 1. Potassium tetranitropalladate (0.01 mmol, 0.037 g) and bpy4dca (0.01 mmol, 0.027 g) were refluxed in a 2 : 1 mixture of acetonitrile to deionised water (15 mL). After 3 h the resulting yellow solution was allowed to very slowly cool to room temperature. As the product complex is only sparingly soluble, thin, needle-like crystals of **1** formed as the reaction mixture cooled. Needle crystals for SCXRD study were collected after the mixture was allowed to stand at room temperature overnight.

NMR (^{1}H, ppm). 8.83 (2H, d, 1.1 Hz), 8.50 (2H, dd, 0.7 Hz, 5.8 Hz), 8.10 (2H, dd, 1.8 Hz, 5.8 Hz), 4.00 (6H, s).

FT-IR (ATR, cm^{-1}). 3061 (w), 2960 (w), 1716 (s), 1616 (w), 1560 (w), 1402 (s), 1348 (s), 1319 (br), 1257 (vs), 1066 (br), 1028 (w), 980 (w), 815 (w), 762 (s), 710 (s).

Powder X-ray diffraction

Variable temperature powder X-ray diffraction (PXRD) data were collected on a Rigaku Gemini A Ultra diffractometer using an Atlas CCD detector and an Enhance Ultra CuKα X-ray source (λ = 1.54056 Å). The temperature was controlled with an Oxford Cryosystems Cryojet XL liquid nitrogen flow device. A lightly ground powder sample was loaded onto a Mitegen microloop and data were collected *via* the Powder Pattern tool in CrysAlis^{PRO}.[48] 2D diffraction data were recorded between 2θ = 7° and 50°, with fast rotation of the sample around the φ-axis and the Atlas detector in 1 × 1 binning mode.

Single-crystal X-ray crystallography

Standard single-crystal X-ray diffraction (SCXRD) experiments were performed on the same dual-source Rigaku Gemini A Ultra system described above, now using MoKα radiation (λ = 0.71073 Å). Data collection, indexing and integration procedures were performed with CrysAlis^{PRO}.[48] Structures were solved by dual-space methods using SHELXT,[49] and refined by full-matrix least squares on F^2 using SHELXL.[50]

Photocrystallography

In situ irradiation of the crystal was achieved using modified version of a bespoke LED array,[51] placing 4 LEDs (Kingbright L-7113QBC-D blue LEDs, dominant λ = 465 nm, 16° viewing angle) at a distance of *c.a.* 1 cm away from the crystal in a uniform arc. The design of the LED set-up allows for *in situ* illumination of the crystal without impeding the SCXRD data collection. The LED array was controlled remotely using a Raspberry Pi Zero W computer. An electrical circuit diagram and photograph of the illumination set-up is provided in the ESI,‡ §2. SCXRD data collection and processing were completed as described above. To identify any ES isomer, the photoexcited X-ray data were first refined against the ground state (GS) atomic coordinates by full-matrix least squares on F^2 with SHELXL using a LIST 3 instruction. A Fourier electron density difference map (often called a "photodifference map") was then produced and used to identify new residual features corresponding to the ES isomer. Any significant difference peaks around NO_2 were then used as the basis for a standard disorder refinement in SHELXL using PART instructions, allowing the GS-to-ES isomer ratio to be refined freely from the ES diffraction data in the final model.

Diffuse reflectance measurements

Solid-state diffuse reflectance spectra were collected using an OceanOptics Flame miniature spectrometer and a DH-mini UV-vis-NIR light source. Spectra were collected on evenly-ground powders prepared from pure single-crystals, using the Ocean View control software (version 1.6.5) and data were post-processed using the adjacent-average smoothing method (5 pts). Experimental diffuse reflectance data were converted to absorption profiles using the Kubelka–Munk function:

$$A = \frac{(1-R_\infty)^2}{2R_\infty}$$

where A = calculated absorbance and R = diffuse reflectance.[52]

Density functional theory (DFT) calculations

All DFT calculations were performed with the B3LYP[53,54] hybrid density functional using Gaussian09 (Revision C.01).[55] In the gas phase, geometry optimisations were performed using the quasi-relativistic pseudopotential and associated basis set (SDD) for palladium and a 6-311+G(d) basis set for all other atoms. Frequency calculations to confirm the nature of the stationary points, molecular orbitals, electronic transitions (TD-DFT) and single point energies ("tight" convergence criteria) were all calculated at the optimised geometries using the same basis set combination. Molecular orbitals were visualised using the program Avogadro,[56] while simulated UV/vis spectra were plotted following a standard procedure.[57]

Results and discussion

Crystallisation of 1 and polymorphic transitions

Complex **1** initially crystallises as long, thin yellow needles when the reaction mixture is cooled and then left to stand at ambient temperature overnight. These needle-like crystals were initially used to confirm the structure of **1** by SCXRD at 150 K. Although weakly-diffracting and inherently twinned, the needles were sufficient to confirm the expected atomic connectivity of **1**.

Upon ageing in their supernatant acetonitrile/water mixture at ambient temperature, the needle crystals were observed to undergo a transformation. After 2–3 days, the needles break down into a microcrystalline powder and, on ageing in solution for a further 2–4 weeks, large block-like yellow crystals had formed (Fig. S5, ESI‡). Structure determination of this block morphology by SCXRD confirmed that the chemical structure of **1** remains unchanged, but the crystal structure has transformed to a second polymorphic form.

Aging a dry sample of the needle crystals for the same time period showed no change in the crystal habit, indicating that **1** undergoes a solvent-mediated polymorphic transformation. Attempts to reproduce this solvent-mediated phase transition through repeat crystallisation experiments gave mixed results. While all batches initially formed the expected long needles, herein assigned as metastable polymorph I, which break down into the microcrystalline powder over a few days in solution, growth of the large, block-like crystals of polymorph II was not consistent. In some vials, thicker needle crystals were observed instead of blocks, which were also confirmed as polymorph II by SCXRD. These observations indicate that the formation and crystal growth of polymorph II is very sensitive to the

crystallisation conditions, with the observed variation in crystal size and habit possibly attributable to subtle changes in the concentration of **1** in each crystallisation batch.

PXRD experiments were run to further investigate the phase transition series. A dry sample of **1**, isolated immediately after crystallisation, was analysed at 150 K. Comparison of the experimental PXRD pattern to simulated patterns for forms I and II (Fig. S6, ESI‡) indicates that the precipitated sample contains a mixture of form I and II crystals, even when isolated at this early stage. This shows that there is already some form II present at, or soon after, precipitation of **1** from the reaction mixture, which can then template the complete form I → form II transformation in solution over time. Finally, PXRD of the microcrystalline powders obtained on needle breakdown after 2–3 days in solution confirmed these samples to contain polymorph II only (Fig. S7, ESI‡). This confirms that the I → II phase transition occurs at this stage, regardless of whether larger form II blocks are later obtained.

Ground-state (GS) crystal structures

Ground state (GS) crystal structure of polymorph I. The single-crystal X-ray structure of the metastable polymorph I of **1** at 150 K is summarised in Fig. 1 and Table 1. Form I crystallises in the triclinic space group $P\bar{1}$, with two molecules of **1** in the asymmetric unit (Z' = 2). In both molecules the Pd(II) centre adopts a strained square planar geometry, due to the bite angle of the chelating bpy4dca ligand (molecule **a**, angle N(3)–Pd(1)–N(4) = 79.8(6)° and RMS deviation of 0.0477 from the plane for Pd(1), N(1), N(2), N(3) and N(4); molecule **b**, angle N(7)–Pd(2)–N(8) = 79.5(6)° and RMS deviation of 0.0502 from the plane for Pd(2), N(5), N(6), N(7) and N(8)). In both molecules, the nitrite ligands adopts solely nitro-(η^1-NO_2) coordination geometry in this ground state (GS) structure. The diffraction data quality for form I is not that high, reflecting the fact that form I crystallises as thin needles that produce only limited diffraction intensity and are inherently twinned. However, the data are sufficient to confirm the atomic connectivity and the standard uncertainties on the bond distances and angles are reasonable enough to allow fair comparison between datasets.

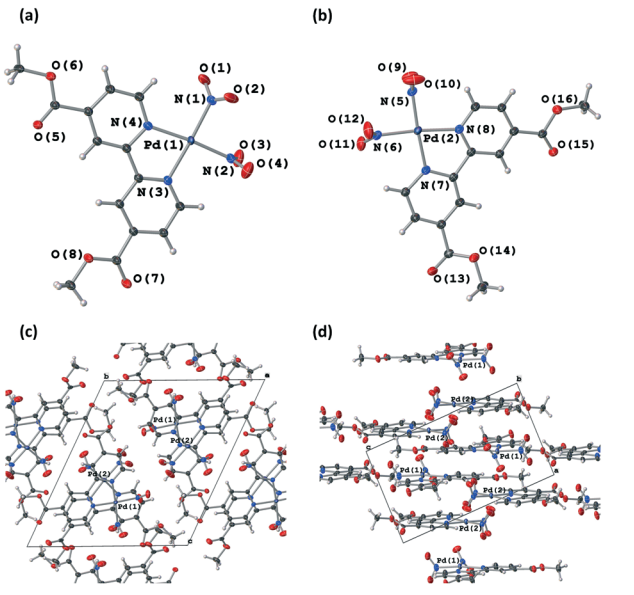

Fig. 1 Single-crystal X-ray structures showing the atomic connectivity for molecule **a** (a) and molecule **b** (b) of **1** in polymorph I, with ellipsoids shown at 50% probability and crystal packing diagrams for polymorph I, viewed along [100] (c) and [010] (d), with Pd(II) centres labelled to illustrate stacking.

Ground state (GS) crystal structure of polymorph II. The single crystal X-ray structure of form II was also obtained at 150 K (Fig. 2, Table 1). This polymorph crystallises in the monoclinic space group $P2_1/n$ with one complex molecule in the asymmetric unit (Z' = 1). The Pd(II) centre again adopts a slightly strained square planar geometry due to the coordination demands of bpy4dca, although the geometry is less strained than the molecules in polymorph I (angle N(3)–Pd(1)–N(4) = 80.5(1)° and RMS deviation of 0.0250 from the plane for Pd(1), N(1), N(2), N(3) and N(4)). Both nitrite ligands again adopt solely nitro-(η^1-NO_2) coordination in this 150 K GS structure.

Comparison of polymorphs I and II. As expected, forms I and II show significant differences in their crystal packing. In form I, the planar molecules pack in a sheet, or β-type, arrangement with sheets then stacked perpendicularly (Fig. 1(c)). The crystallographically independent molecules **a** and **b** stack alternately with an ababab⋯motif (Fig. 1(d)), and are rotated by *ca.* 130° with respect to one another. There are no obvious π–π stacking interactions between **a** and **b** and the Pd(II) atoms are offset with one another, with a Pd(1)⋯Pd(2) distance of 3.813(2) Å. Conversely, form II adopts a flattened herringbone (or γ-type) packing arrangement, with alternating stacks of molecules rotated with respect to one another (Fig. 2(b)).

Crystal Explorer fingerprint plots can be used to give a visual representation of the differences in the intermolecular interactions, and so crystal packing environments, between the polymorphs.[58,59] A full set of fingerprint plots for each of the 3 crystallographically independent molecules are given in the ESI‡ (Table S2), and highlight the key interactions in each polymorph. The fingerprint plots are similar in shape for all molecules and intermolecular contacts in both polymorphs. The key difference between the molecules appears to involve the C⋯H contacts, with form I molecule **a** involved in considerably shorter and stronger C⋯H contacts compared to molecule **b** and polymorph II. This results from a short contact between the H(14B) on a methyl group and C(2) in pyridine in a neighbouring **a** molecule.

Overlays of the independent molecules of **1** in polymorph I (**a** and **b**) with that of polymorph II using the CCDC software Mercury[60] also give an indication of the differences in the molecular geometry between the different crystal forms (Table S3‡). Comparison of polymorph I molecule **a** with

Table 1 Single crystal X-ray data for **1** at 150 K. Polymorph I ground state GS and photostationary excited state ES (λ = 465 nm), polymorph II ground state GS and photostationary excited state ES (λ = 465 nm)

	Poly I (GS)	Poly I (ES)	Poly II (GS)	Poly II (GS)
Irradiation time (λ = 465 nm)/min	0	480	0	240
X-ray radiation wavelength/Å	0.71073	0.71073	0.71073	0.71073
Empirical formula	$C_{14}H_{12}N_4O_8Pd_1$	$C_{14}H_{12}N_4O_8Pd_1$	$C_{14}H_{12}N_4O_8Pd_1$	$C_{14}H_{12}N_4O_8Pd_1$
Formula weight	470.68	470.68	470.68	470.68
Temperature/K	150	150	150	150
Crystal system	Triclinic	Triclinic	Monoclinic	Monoclinic
Space group	$P\bar{1}$	$P\bar{1}$	$P2_1/n$	$P2_1/n$
a/Å	8.4976(9)	8.4570(17)	8.4629(3)	8.5145(3)
b/Å	13.812(2)	13.863(2)	7.7277(3)	7.8127(3)
c/Å	15.5449(19)	15.648(4)	24.8938(7)	24.8999(6)
α/°	63.761(14)	63.84(2)	90	90
β/°	82.994(9)	83.505(18)	95.196(3)	93.874(3)
γ/°	78.512(11)	79.366(16)	90	90
Volume/Å^3	1602.5(4)	1617.4(6)	1621.33(10)	1652.59(10)
Z	4	4	4	4
ρ_{calc}/g cm^{-3}	1.951	1.933	1.928	1.892
μ/mm^{-1}	1.215	1.204	1.201	1.178
F(000)	936	936	936	936
Crystal size/mm	0.25 × 0.05 × 0.02	0.25 × 0.05 × 0.02	0.3 × 0.2 × 0.1	0.3 × 0.2 × 0.1
Reflections (independent)	6168 (3599)	6230 (2439)	6851 (3315)	6854 (3383)
Goodness of fit on F^2	0.956	0.920	1.019	1.024
R_{int}	0.0978	0.1327	0.0425	0.0372
R_1 [$I \geqq 2\sigma(I)$]	0.0764	0.1072	0.0393	0.0435
wR_2 [all data]	0.2454	0.3464	0.0780	0.0917
Largest difference peak and hole/e Å^{-3}	1.80 and −1.15	1.82 and −1.31	0.77 and −0.61	0.99 and −0.99

form II shows the geometry is largely similar, with a RMSD of 0.1712 across the whole molecule. The most significant deviations involve the methyl groups of the ester, with a maximum displacement of 0.38 Å. Comparing form I, molecule **b** with form II, the RMSD is slightly larger at 0.3006, with more significant deviations in the NO_2 ligands, as well as the methyl ester groups.

Choice of excitation wavelength

As our prior experience indicated that linkage isomer complexes containing strong chromophores often display little or no photoswitching, care was taken when designing photocrystallography experiments with **1**, particularly in selecting the excitation source wavelength. It is also known that where the ES absorbs at the chosen excitation wavelength it is possible to both populate and depopulate the ES on irradiation, creating a photostationary equilibrium that limits the maximum ES population that can be achieved.[44,61] Thus, the choice of excitation wavelength is key. To help guide wavelength choice, the diffuse reflectance spectrum was collected on a lightly ground powder sample of as-synthesised **1**, confirmed by PXRD to contain a mixture of forms I and II (Fig. S6‡). The absorption profile, obtained using the Kubelka–Munk transform (Fig. 3), was used to select suitable excitation wavelengths. The high absorption recorded between 250 and 425 nm indicates that excitation wavelengths in this region will be strongly absorbed by the complex, while wavelengths outside the absorption band

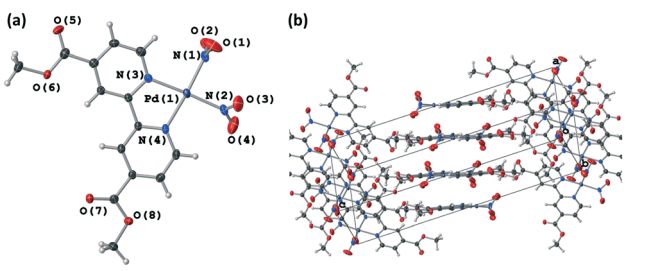

Fig. 2 (a) Single-crystal X-ray structures showing the atomic connectivity **1** in polymorph II, with ellipsoids shown at 50% probability and (b) crystal packing diagram for polymorph II illustrating the γ-type flattened herringbone packing arrangement.

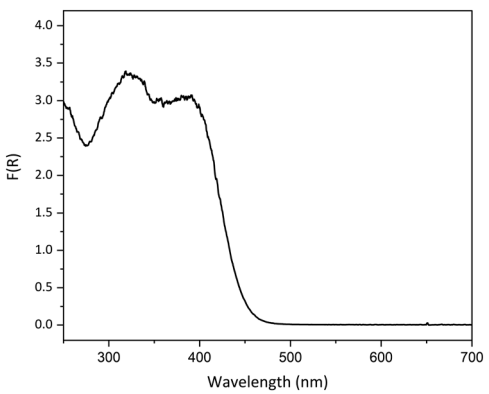

Fig. 3 Solid-state absorption profile for a powdered sample of as-synthesised crystals of **1**, converted from the experimental diffuse reflectance spectrum using the Kubelka–Munk transformation.

(>500 nm) are not expected to promote linkage isomerism. Prior research has indicated that selecting a wavelength in the tail of the absorption band helps to maximise the penetration of the excitation light through the single crystal, thereby maximising the measured level of photoactivation.[62,63]

To test this hypothesis for **1**, and to ensure a suitable range of excitation conditions were trialled, a series of preliminary experiments were first run with a well-diffracting crystal of polymorph II. A crystal was irradiated for 1 h at 150 K, using 4 different LED wavelengths across the absorption profile: 390 nm, 405 nm, 465 nm and 500 nm, after which time a steady-state photocrystallography dataset was collected. The results of these preliminary studies are summarised in Table S4.‡

For near-UV wavelengths (390 nm, 405 nm) no change in the coordination of the nitro-(η^1-NO_2) ligands could be discerned from the photodifference map, however the crystal quality and diffraction intensity was observed to decrease with exposure to both wavelengths and particularly at λ = 390 nm. Irradiation at λ = 500 nm similarly showed no excitation in either nitrite ligand, but at this wavelength the crystal quality remained high following irradiation. Finally, irradiation at λ = 465 nm produced a significant change in the photodifference map, with both nitrite ligands found to photoswitch from GS nitro-(η^1-NO_2) to above 50% of the ES *endo*-nitrito-(η^1-ONO) isomer. These results agree with prior research[62,63] and a possible explanation is that wavelengths near the maxima of the absorption peak (λ = 390 nm and 405 nm) are too strongly absorbed in the outer layers of the crystal, limiting the transmission of excitation light through the sample and causing the observed crystal damage. Conversely, choosing a wavelength in the tail of the absorption band can help minimise crystal damage, while simultaneously promoting photoisomerisation to a high conversion percentage due to the improved penetration depth of the excitation light through the crystal bulk. Finally, the observation that a wavelength entirely outside the absorption maximum (500 nm) induced no change in the nitrite ligand geometry or the crystal quality is unsurprising and indicates that light of too low energy cannot produce any significant photo-response.

Steady-state photocrystallography at λ = 465 nm

Photoexcitation of form II at 150 K. Building on the preliminary excitation tests, form II was first subject to a steady-state photocrystallographic study at 150 K. A crystal was mounted at 150 K and a SCXRD dataset obtained in the dark to confirm the GS structure. The same crystal was then irradiated at λ = 465 nm, *in situ* on the diffractometer. The irradiation was stopped at regular intervals and a complete SCXRD experiment was run to determine the level of conversion to the metastable ES as a function of irradiation time. These results are shown in Fig. 4. As for the preliminary excitation tests, formation of a photoinduced nitrito-(η^1-ONO) linkage isomer was observed, reaching a maximum occupancy of 71% in nitrite ligand #1 and 68% in nitrite ligand #2 after 4 h irradiation at 150 K. SCXRD data for this photostationary state are provided in Table 1.

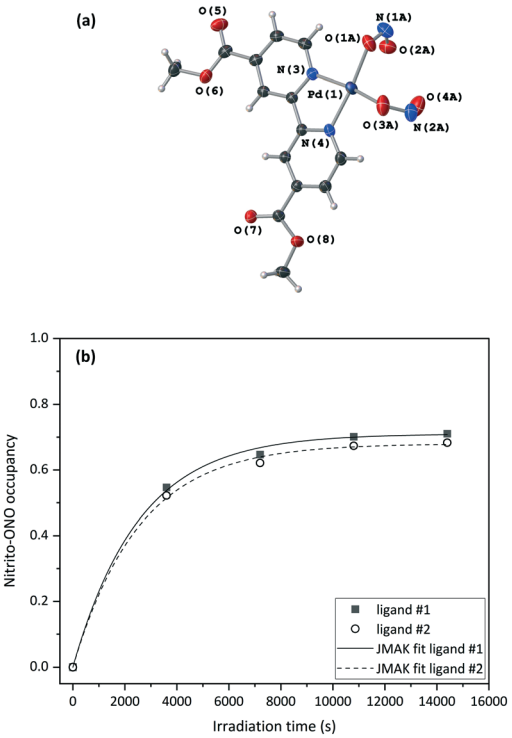

Fig. 4 (a) Single-crystal X-ray structure showing the ES nitrito-(η^1-ONO) isomer in the photostationary state of form II of **1** at 150 K, (b) ES nitrito-(η^1-ONO) in polymorph II of **1** as a function of irradiation time with λ = 465 nm at 150 K; for ligand #1 α_0 = 0, α_∞ = 0.71, n = 1 and a value of k = (0.392 ± 0.017) × 10^{-3} s^{-1} was refined from the data (R^2 = 0.9985); for ligand #2 α_0 = 0, α_∞ = 0.68, n = 1 and a value of k = (0.392 ± 0.016) × 10^{-3} s^{-1} was refined from the data (R^2 = 0.9987).

Fig. 4(a) and S8‡ show that the crystal structure remains largely unchanged on photoactivation, excepting the change in nitrite binding mode. An increase in the unit cell volume of 1.93% was found on excitation, which is a fairly large change compared with other photoactive linkage isomers.[36,38,43,45]

The excitation profiles for both ligands in Fig. 4(b) are sigmoidal, as seen for similar linkage isomer crystals.[38,45,64] To extract kinetic information on the population dynamics of the GS → ES reaction, the excitation profiles can be fitted to the Johnson–Mehl–Avrami–Kolmogorov (JMAK) kinetic model:[65–67]

$$a(t) = a_\infty + (a_0 - a_\infty)\exp[-kt^n]$$

where $\alpha(t)$ is the time-dependent population of the excited state, α_0 and α_∞ are the initial and final ES populations, k is the rate constant, and n is the Avrami exponent. n is related to the dimensionality D of the transformation as $D = n - 1$. Our previous work with linkage isomer materials has shown that a value of n = 1 is typical for these reactions, *i.e.*

nucleation of the photoexcited phase is homogeneous through the crystal bulk.[29] As such, n was fixed at 1 for all analyses. The value of k refined from the data was almost identical for both nitrite ligands and indicates that the photoreaction proceeds similarly at each independent nitrite site in the crystal lattice.

Variable temperature parametric studies were next run to determine the point at which the ES is no longer metastable. The photoinduced nitrito-(η^1-ONO) isomer occupancy remains stable up to 210 K, at which temperature the ES begins to decay thermally back to the GS arrangement for both nitrite ligands #1 and #2 (Table S5‡).

Photoexcitation of form II at 200 K. Our results with other Pd–nitrite linkage isomers have shown that the maximum level of ES photoconversion achieved in the crystal can be sensitive to the experiment temperature, particularly when the photoswitching ligand is restricted by hydrogen bonds in the GS.[37] As such, a second steady-state photocrystallography experiment was run with polymorph II at 200 K, a temperature just below the "metastable limit" observed for this system (see Table S5‡).

A crystal was mounted at 200 K and a GS structure was first obtained in the dark at this temperature (Table 2). The GS structure is similar to that obtained at 150 K, with the exception that nitro-(η^1-NO_2) ligand #2 displays some disorder that was modelled in all datasets collected at this higher temperature (Fig. S9‡). The same crystal was then irradiated *in situ* on the diffractometer, with the irradiation paused and SCXRD datasets collected at regular intervals to obtain the photoexcitation profile for the crystal at 200 K. In line with other studies,[37] the nitrito-(η^1-ONO) isomer population level increased at higher temperature, with maximum ES occupancy levels of 80% for nitrite ligand #1 and 70% for nitrite ligand #2 in the 200 K photostationary state.

As for the 150 K experiments, the excitation profile at 200 K was fitted to the JMAK model, allowing the extraction of kinetic information. The difference between the values of k at the two different nitrite positions is just statistically significant. However, if errors on the experimental values – for example the error on the temperature measurement from the cryostream – are also taken into account, then the difference between these k values is small enough that they can still be considered to be similar. However, data fitting showed that the photoreaction proceeds more slowly at higher temperature, with smaller rate constants k of $(0.227 \pm 0.004) \times 10^{-3}$ s^{-1} (ligand #1) and $(0.198 \pm 0.006) \times 10^{-3}$ s^{-1} (ligand #2) at 200 K, compared to $(0.392 \pm 0.017) \times 10^{-3}$ s^{-1} (ligand #1) and $(0.392 \pm 0.016) \times 10^{-3}$ s^{-1} (ligand #2) 150 K. It also took a much longer time (10 h) to reach the photostationary state at 200 K than it did at 150 K. This result is to be expected, as it is known that the nitro and nitrito isomers are subject to a thermodynamic equilibrium.[29] At any temperature, the forwards nitro → nitrito photoreaction is in competition with the thermally-activated nitrito → nitro back-reaction. Thus, the reverse nitrito → nitro process is more favoured and so occurs at a faster rate at 200 K than at 150 K, causing the rate of the forwards nitro → nitrito photoreaction to be slower at the higher temperature.

Variable temperature parametric studies conducted for the photoexcited state obtained at 200 K showed similar results to the 150 K photocrystallography study, with decay of the ES measurable by 210 K.

Pseudo-steady-state experiments with form II. The design of the bespoke LED ring array allows the LEDs to remain on and in position whilst SCXRD data is collected simultaneously. This enabled pseudo-steady-state photocrystallographic data to be collected for form II, providing insight into the suitability of **1** for applications that may require the crystal to be continuously illuminated. A new crystal was first irradiated for a period of 6 h, as this is the point at which the photostationary state is achieved in Fig. 5. The LEDs were then left on and *in situ* SCXRD datasets were obtained at intervals between 200 and 250 K. These pseudo-steady-state photocrystallographic data are summarised in Table S6.‡ Despite a total irradiation time of the crystal of more than 20 h, the SCXRD data showed no appreciable levels of crystal decay, indicating that polymorph II crystals of **1** are robust to irradiation at λ = 465 nm. Fig. S10‡ shows that under continuous illumination the ES nitrito-(η^1-ONO) could still be detected *via* a standard crystallographic experiment up to 240 K (−33 °C). Our time-resolved experiments with similar Pd(II)–nitrite systems indicate that the ES in **1** is likely to be detectable with faster X-ray or spectroscopic methods to higher temperatures,[29] and

Table 2 Single crystal X-ray data for **1** at 200 K. Polymorph II ground state GS and photostationary excited state ES (λ = 465 nm)

	Poly II (GS)	Poly II (ES)
Irradiation time (λ = 465 nm)/min	0	600
X-ray radiation wavelength/Å	0.71073	0.71073
Empirical formula	$C_{14}H_{12}N_4O_8Pd_1$	$C_{14}H_{12}N_4O_8Pd_1$
Formula weight	470.68	470.68
Temperature/K	200	200
Crystal system	Monoclinic	Monoclinic
Space group	$P2_1/n$	$P2_1/n$
a/Å	8.5278(3)	8.5715(4)
b/Å	7.7446(3)	7.8480(4)
c/Å	24.9228(8)	24.9357(13)
α/°	90	90
β/°	95.023(3)	93.900(5)
γ/°	90	90
Volume/Å^3	1639.69(10)	1673.52(15)
Z	4	4
ρ_{calc}/g cm^{-3}	1.907	1.868
μ/mm^{-1}	1.187	1.163
F(000)	936	936
Crystal size/mm	0.3 × 0.2 × 0.1	0.3 × 0.2 × 0.1
Reflections (independent)	7216 (3345)	7306 (3414)
Goodness of fit on F^2	1.033	1.014
R_{int}	0.0399	0.0487
R_1 [$I \geq 2\sigma(I)$]	0.0382	0.0482
wR_2 [all data]	0.0804	0.0956
Largest difference peak and hole/e Å^{-3}	0.65/−0.57	0.89/−0.96

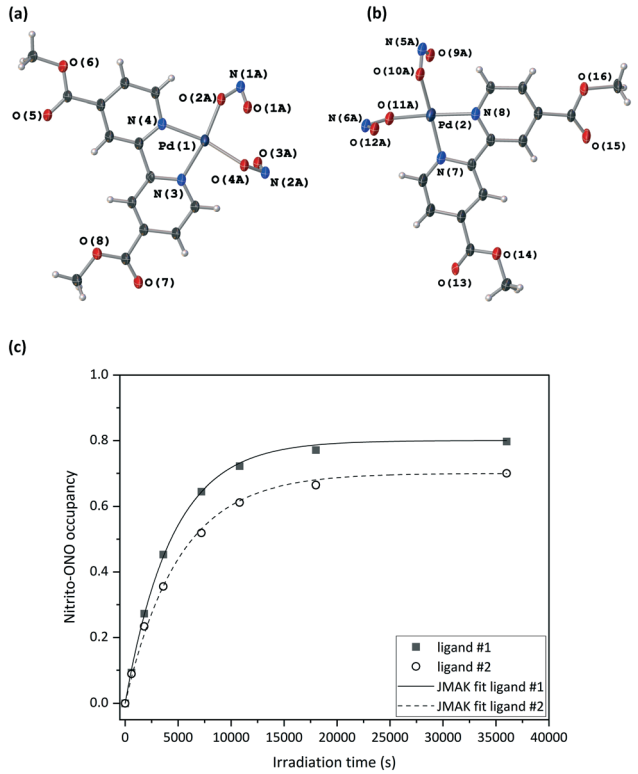

Fig. 5 (a) Single-crystal X-ray structure of the ES nitrito-(η^1-ONO) isomer in the photostationary state of form I, molecule **a** of **1** at 150 K, (b) single-crystal X-ray structure of the ES nitrito-(η^1-ONO) isomer in the photostationary state of form I, molecule **b** of **1** at 150 K, (c) ES nitrito-(η^1-ONO) in polymorph II of **1** as a function of irradiation time with λ = 465 nm at 200 K; for ligand #1 α_0 = 0, α_∞ = 0.80, n = 1 and a value of k = (0.227 ± 0.004) × 10^{-3} s^{-1} was refined from the data (R^2 = 0.9993); for ligand #2 α_0 = 0, α_∞ = 0.70, n = 1 and a value of k = (0.198 ± 0.006) × 10^{-3} s^{-1} was refined from the data (R^2 = 0.9978).

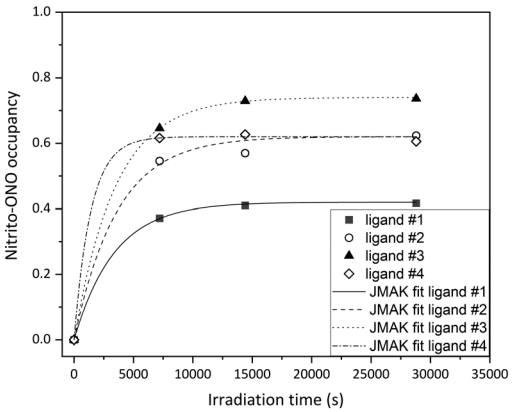

Fig. 6 ES nitrito-(η^1-ONO) in polymorph I of **1** as a function of irradiation time with λ = 465 nm at 150 K; for ligand #1 α_0 = 0, α_∞ = 0.42, n = 1 and a value of k = (0.297 ± 0.008) × 10^{-3} s^{-1} was refined from the data (R^2 = 0.9998); for ligand #2 α_0 = 0, α_∞ = 0.62, n = 1 and a value of k = (0.277 ± 0.037) × 10^{-3} s^{-1} was refined from the data (R^2 = 0.9936); for ligand #3 α_0 = 0, α_∞ = 0.74, n = 1 and a value of k = (0.287 ± 0.003) × 10^{-3} s^{-1} was refined from the data (R^2 = 0.9999); for ligand #4 α_0 = 0, α_∞ = 0.62, n = 1 and a value of k = (0.707 ± 0.342) × 10^{-3} s^{-1} was refined from the data (R^2 = 0.9991).

indicates that these materials are close to meeting the requirements for useful, near-room temperature operation in real-world devices.

Photoexcitation of form I at 150 K. Though the limited diffraction intensity available from crystals of form I precluded their study at 200 K, it was possible to perform some photocrystallographic studies at 150 K with this polymorph. A crystal of form I was first mounted on the diffractometer at 150 K and a SCXRD dataset collected in the dark to confirm the GS structure. The same crystal was then irradiated *in situ*, with irradiation stopped at regular intervals to allow collection of SCXRD data. The results of these experiments are given in Fig. 6 and S11‡ and Table 1.

All four crystallographically independent nitrite ligands in form I are found to undergo nitro → nitrito photoisomerisation, with a photostationary state achieved after 8 h irradiation. The final excitation levels at each nitrite position are more varied in form I, with maximum ES occupancies of 42% for ligand #1, 62% for ligand #2, 74% for ligand #3 and 62% for ligand #4.

As for polymorph II, the crystal structure of form I remains largely unchanged on photoactivation, excepting the change in the nitrite ligand coordination. A moderate increase of 0.93% in the unit cell volume between the GS and photostationary ES was observed, which is considerably smaller than that seen for form II and is more in-line with other nitrite linkage isomers that display incomplete photoswitching in the single-crystal.[43,45]

The excitation profiles for all four nitrite ligands were fitted to the JMAK model, providing kinetic information (Fig. 6). The values of k refined from the data indicate that the reaction rates are similar for ligands #1, #2 and #3 when statistical errors are taken into account. Conversely, the analysis for ligand #4 indicates that the photoreaction here proceeds more quickly, with a value of $k > 2\times$ larger than at the other sites. However, it should be noted that the error on this value is very high and it is therefore unreliable. More data points between 0 h and 2 h irradiation would be necessary to confirm whether nitro → nitrito switching proceeds more quickly in ligand #4 compared with ligands #1–#3.

Finally, variable temperature parametric studies following the decay of the ES in form I were not possible as the diffraction intensity from the needle crystals was too weak at elevated temperatures.

Rationalising the photoresponse of 1

An attempt to rationalise the photoexcitation behaviour of **1** can be made by considering the photoreaction kinetics, the steric influences on the nitrite ligands from the surrounding crystal environment, and the electronic structure and resulting photophysical properties. Comparison can be made both between the individual nitrite ligand sites and also between the different polymorphic forms.

Comparison of individual nitrite ligand sites. First, we note above that there is little significant difference in the rate of nitro → nitrito isomerisation at distinct nitrite sites in the same crystal structure. Conversely, the maximum ES population level varies significantly at each site, particularly in polymorph I. One way to rationalise the different photoresponses at each nitrite site, in terms of their respective crystal structures, is to compare the intermolecular interactions that are formed by each ligand. It is previously shown that hydrogen bonds involving the GS nitro-(η^1-NO_2) can influence the maximum ES population that is achieved, as these hydrogen bonds must be broken to allow the atoms to rearrange.[37] While **1** contains no strong hydrogen bond donors, CrystalExplorer fingerprint plots confirm the existence of weak C–H···O hydrogen bonds for both polymorphs and a summary of these interactions for each polymorph and nitrite ligand site is provided in Table S7 and Fig. S12.‡ All interactions can be classified as moderate or weak on the basis of their donor–acceptor distance and directionality[68] and thus should not require large amount of energy to overcome. This supports the fact that excitation is seen for all ligands. There is no clear trend between the number, bond length or directionality of C–H···O interactions and the ES population level achieved at each nitrite site, indicating that C–H···O contacts alone do not adequately explain the photoresponse at the individual nitrite ligand sites for either polymorph.

C–H···O bond analysis does help to rationalise the increase in photoactivity in form II on warming, however (Table S8‡). All intermolecular C–H···O contacts are found to lengthen significantly at 200 K, while the D–H···A bond angle typically remains similar or becomes more acute. This is consistent with a weakening of the hydrogen bonding interactions, which can serve to facilitate the higher levels of photoactivation observed in form II crystals at higher temperature and is consistent with behaviour reported for other, related crystal systems.[37]

After photoswitching, the ES nitrito ligands will (re)form new close-contacts and it is feasible that the ES geometry adopted may be driven, in part, by the formation of stabilising interactions to nitrito-(η^1-ONO). Fig. S13 and Table S9‡ summarise the key interactions involving the photoexcited ligands in I and II. As for the GS, no obvious trends in the C–H···O interactions arise that can account for the observed ES population levels at each nitrite site.

A final way to rationalise the photoresponse at each ligand site, in terms of structure, is to consider topochemical factors. It has long been understood that solid-state reactions should be topotactic, *i.e.* they will proceed in a way that minimises the amount of atomic or molecular movement in the structure.[69,70] The application of these ideas to **1** dictates that the nitrite ligand most likely to achieve the highest level of photoswitching in the single crystal is the one that requires the smallest change in its surrounding crystalline environment. A common way to assess the impact of the local crystalline environment on nitro → nitrito switching is to utilise the "reaction cavity" concept.[25,26] A comparison of the available reaction cavity volume, V_c, at each nitrite site provides an assessment of the space available for the required atomic rearrangements. It would be expected that, for a topotactic transformation, a large V_c will correlate with a high photoconversion to the nitrito-(η^1-ONO) isomer. An estimation of V_c for each of the individual nitrite groups in the GS structures of forms I and II was made using the void space calculation tool in Mercury (further details of this procedure are included in the ESI‡).[60] The results of the reaction cavity analyses for individual nitrite sites are given in Table 3. There is a trend between the GS V_c and the nitrito-(η^1-ONO) population achieved, in that the nitrite site with the lowest ES population (form I ligand #1, 45%) has the smallest V_c at 24.34 Å^3, while all other sites achieving higher ES population levels (60–80%) have much larger V_c. However, there is poor correlation among the ligand sites in the higher ES population bracket (Fig. S14‡).

Comparing the reaction cavities for form II at 150 and 200 K (Table S10‡) shows no significant trend between V_c and the ES population level, indicating that the reaction cavity concept does not explain the increase in photoactivity on warming.

All of the above observations highlight the limitations of rationalising ES population levels with respect to steric factors alone, particularly for crystals containing multiple isomerising ligands. In both forms I and II it is likely that ES conversion at one site will influence switching at other sites in that crystal (either *via* induced steric strain or due to the rearrangement of influential intermolecular interactions). Thus, it is impossible to deconvolute the effects of excitation at multiple sites when analysis is limited to static, photostationary X-ray structures.

Comparison between polymorphs. Firstly, a comparison of k for forms I and II at 150 K indicates that the reaction proceeds more quickly for form II than form I, although the values are of the same order of magnitude. The average value of k for form II nitrite ligands #1 and #2 is $(0.392 \pm 0.023) \times 10^{-3}$ s^{-1}, while for form I nitrite ligands #1, #2 and #3 it is $(0.287 \pm 0.038) \times 10^{-3}$ s^{-1} (note that k for form I ligand #4 was omitted from this analysis due to its large uncertainty). This is interesting, as a comparison of the crystal size and habit between polymorphs would suggest a faster reaction for I than II. The kinetic analysis therefore indicates that the reaction rate is not only influenced by the penetration of the excitation light through the crystal bulk.

On assessing the effect of the differing crystal packing environments in I and II, it is interesting to first compare the ES structures adopted in each form. Inspection of Fig. 4(a) and 5(a) and Table S11‡ shows that a different ES molecule is accessed in each polymorph. In form II, the two nitrito-(η^1-ONO) ligands coordinated to Pd(1) point in the same direction (*i.e.* both "up" in relation to the Pd(1), N(1), N(2), N(3), N(4) square plane). By contrast, the form I ES molecule contains two nitrito-(η^1-ONO) ligands oriented in opposing directions (*i.e.* one "up", one "down" in relation to the square

Table 3 Reaction cavity (V_c) analysis for individual nitrite sites in **1** polymorphs I and II at 150 K. V_c was estimated by removing the target nitrite group and performing a contact surface void space calculation in Mercury (probe radius 1.2 Å, grid spacing 0.1 Å)

Polymorph	Nitrite ligand #	Nitrito-ONO occupancy	V_c per unit cell (Å^3)	V_c per molecule[a] (Å^3)
I	#1	0.42	48.86	24.43
I	#2	0.62	75.30	37.65
I	#3	0.74	67.78	33.89
I	#4	0.62	80.48	40.24
II	#1	0.71	148.31	37.08
II	#2	0.68	141.44	35.36

[a] V_c per molecule was obtained by dividing the value obtained per unit cell by Z for each structure, allowing direct comparison of reaction cavities for forms I and II.

plane). Reaction cavity analysis (Table 3) makes no clear distinction in the volumes occupied by "up" or "down" ligands; thus, it is unlikely that the geometry preference is governed by steric crowding in the crystal lattice. Assessment of C–H···O interactions also provides no real insight into the geometry preference: for all ligands it is possible to identify alternative C–H donors had the nitrito ligand oriented itself in the opposing direction. It is likely instead that the combined sum of all weak intermolecular interactions make one ES geometry more favourable than the other in each case.

Finally, it can be said that the photoreaction in form II is more efficient than in form I: not only does it proceed more quickly, but a higher over ES population level is achieved when averaging across all nitrite sites. Reaction cavity analyses for assessing the crystal structures as a whole, rather than taking isolated cavities for individual ligands, provide a better rationale for these observations: for polymorph I, a total V_c of 282.48 Å^3 is calculated for the unit cell, whereas form II displays a larger overall V_c of 287.45 Å^3 indicating that, where crystals contain multiple isomerisable groups, it is more accurate to consider the reactions cavities as a whole across the full crystal structure.

Density functional theory (DFT)

Finally, gas-phase DFT calculations were used to further explore the molecular and electronic structures of **1** in each polymorph.

The geometries of form I molecules **a** and **b** and the lone molecule of **1** in form II were first optimised [DFT(B3LYP)/6-311+G(d) for light atoms, DFT(B3LYP)/SDD for Pd], starting from the GS SCXRD structures. Interestingly, form I molecules **a** and **b** both optimise to the same geometry, with identical single point energies (Fig. S15‡). Comparing the optimised geometry of **1** in forms I and II, subtle differences were still observed, with a RMSD of 0.3996 between molecules but only a small single point energy difference of 1 kJ mol^{-1}. Both optimised geometries are confirmed to be minima by frequency calculations and the key difference is in the orientation of the nitro-(η^1-NO_2) ligands. The ES structures were also optimised from SCXRD structures. Again, form I molecules **a** and **b** optimise to the same geometry and retain the up/down orientation of nitrito-(η^1-ONO) ligands observed experimentally. The optimised ES structure of form II retains the up/up arrangement seen by photocrystallography and calculations indicate that this geometry is only slightly less stable than the up/down arrangement, by 4 kJ mol^{-1}. These calculations reinforce the conclusions of the steric analyses, indicating that solid state interactions in the surrounding crystal structure must influence the geometry preference in each case.

Calculated absorption spectra were also obtained for I and II using TDDFT (Fig. 7). Relative changes in the optical spectra can rationalise the switching behaviour seen experimentally. Fig. 7 shows that there are only subtle differences in the calculated GS absorption profiles between forms I and II, both displaying λ_{max}(GS) = 270 nm, with absorption tailing off by ~500 nm. Despite being calculated in the gas phase, the spectra compare well to the experimental diffuse reflectance spectrum (Fig. 3 and S16‡) and the similarity between forms I and II indicate that subtle differences in molecular geometry have little influence on the absorption properties. The calculated ES spectra for each polymorph differ more significantly than those of the GS, which may be expected given the larger difference in the ES geometries adopted. However, the key difference is the presence of an additional, higher-energy band overlapping with the main absorbance (*ca.* 250 nm), with the spectra

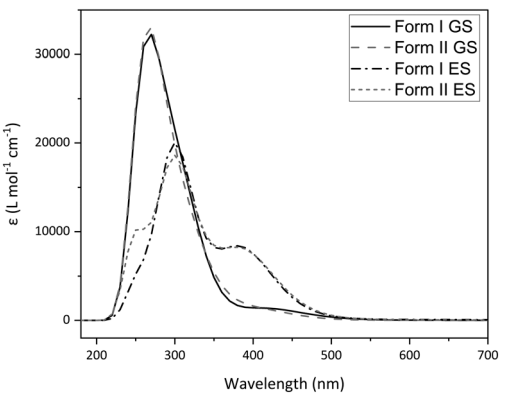

Fig. 7 Calculated absorption spectra for **1** obtained by gas-phase TDDFT, comparing polymorphs I and II in their optimised GS and ES geometries.

again comparing well in the experimental photoexcitation region of 390–500 nm. The key comparison is between the GS and ES spectra, with the ES spectra displaying a significant red-shift in the main absorption maxima ($\Delta\lambda$ = 30 nm, λ_{max}(ES) = 300 nm) in addition to the formation of a new peak centred at 380 nm. This shows that the 465 nm excitation light is absorbed more strongly by the nitrito-(η^1-ONO) ES than it is by the GS, which has implications for ES population levels. If the ES absorbs the excitation light more strongly, then as the outer layers of the crystal are excited these will act as a barrier to photoswitching, preventing the excitation light from penetrating well through the crystal bulk and ultimately limiting the ES population level that can be achieved. This is one possible explanation for the incomplete ES photoconversion seen for both polymorphs of **1**. A second possible explanation is that, as the ES isomer absorbs the 465 nm excitation light, there is also potential for it to also depopulate the ES to some extent, setting up a photostationary equilibrium.[44,61] This would also account for the incomplete photoconversion seen.

Molecular orbitals (MOs) and orbital energies were also calculated for GS molecules and used to assess the electronic transitions required to break the Pd–NO_2 bond and facilitate switching. Initial results showed that forms I and II produce very similar outputs (Fig. S17 and S18‡) and as such the remainder of this analysis uses solely form II. Inspection of the frontier MOs for **1** (Fig. 8) shows the HOMO has a significant contribution from Pd and NO_2 moieties (56% LCAO-MO contribution) and the localisation of electron density across Pd1, N1 and N2 indicates that this is a bonding MO. Conversely, the LUMO is primarily composed of bpy4dca (93%) and has little contribution from either Pd or NO_2. In fact, a significant contribution from Pd and NO_2 is not seen until LUMO+3 (29%) and the localisation of density indicates this is an antibonding-type orbital, with clear nodes between Pd and both NO_2 ligands. The analysis of frontier MOs suggests that the HOMO → LUMO+3 transition will break the Pd–NO_2 bonds and facilitate linkage isomer switching. TDDFT shows that the HOMO → LUMO+3 transition contributes to ESs in the region of 411–431 nm, with strongest contribution to ES #6 (411.39 nm, f = 0.0225, 44% contribution). These outputs (calculated in the gas phase) are slightly blue-shifted compared to the wavelengths used for solid state switching.

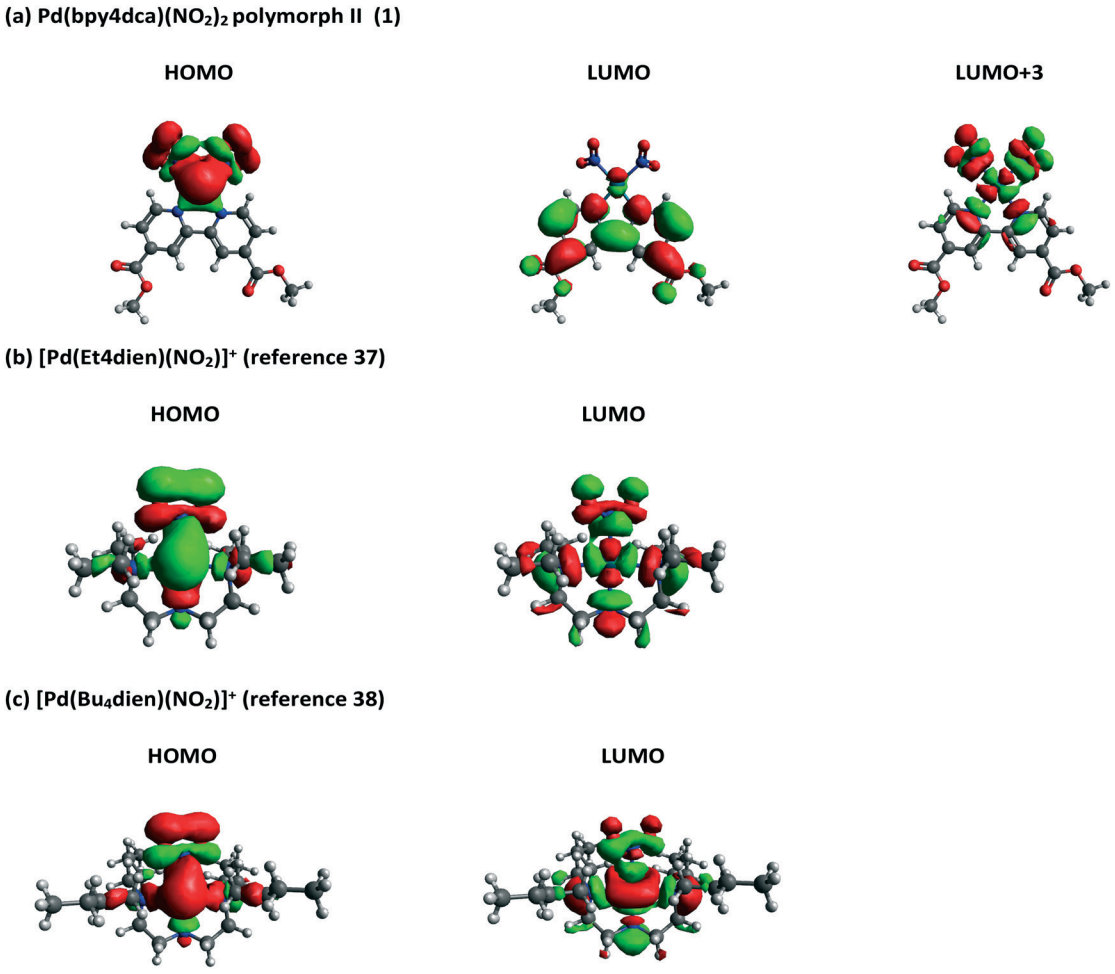

Fig. 8 Calculated frontier molecular orbitals for (a) **1** (polymorph II) and two other Pd(II)–nitrite molecules reported in the literature, capable of 100% conversion to a nitrito-(η^1-ONO) excited state: (b) $[Pd(Et_4dien)(NO_2)]^+$,[37] and (c) $[Pd(Bu_4dien)(NO_2)]^+$.[38]

These MO calculations are most interesting when compared to other Pd(II)–nitrite linkage isomer complexes published in the literature. The frontier MOs for two compounds capable of 100% nitro → nitrito switching, $[Pd(Bu_4dien)(NO_2)]^+$,[38] and $[Pd(Et_4dien)(NO_2)]^+$,[37] are shown in Fig. 8, while three further complexes capable of lower ES photoconversion are included in the ESI‡ (Fig. S19–S23).[71] For all other Pd(II)–nitrite systems reported, MO contributions and localisation of electron density indicates that the main HOMO → LUMO transition is most likely to cause Pd–NO_2 bond-breaking, in contrast to **1**. The presence of the strong chromophore bpy4dca in **1** clearly inserts other, accessible LUMOs between the desired MOs for Pd–NO_2 bond-breaking, making it difficult to access the transition required for linkage isomerism in these systems. This rationale may explain why it was previously challenging to design effective linkage isomer switches that contain strong chromophores as co-ligands.

Conclusions

This study has confirmed by photocrystallography that complex **1**, $[Pd(bpy4dca)(NO_2)_2]$ shows the highest level of nitro → nitrito photoconversion recorded to-date for a nitrite linkage isomer complex containing a co-ligand that is, in itself, a strong chromophore. Informed selection of the appropriate excitation conditions leads to a maximum of 80% ES population in form I. DFT studies provide some rationale the observed photophysical properties of **1** and most interestingly confirm that the presence of the aromatic bpy4dca ligand causes a re-ordering of frontier MOs compared to other Pd(II) linkage isomer materials that do not contain co-ligands with extended pi-systems. This explains why it can be harder to access the transition required for linkage isomer switching in the presence of aromatics, insight that can be applied in future to design a wider variety of linkage isomer switches for new and varied applications.

Single-crystal and PXRD studies also confirm that **1** exists in two different polymorphic forms, I and II, and that irreversible conversion of I into II occurs when form I needles are aged in their supernatant solution for a few days. Both polymorphs are confirmed to undergo photoinduced linkage isomer switching, with photocrystallographic kinetic studies showing that the overall photoreaction is more efficient in form II than form I.

As seen previously by us,[45] and others,[72] the independent nitrite ligand sites in both forms achieve different maximum photostationary ES populations, a factor that must be affected, at least in part, by the crystal packing environment at each site. Despite this, weak C–H···O hydrogen bond analysis is insufficient to explain the trends in photoactivity between sites, either in terms of preferred ES geometry or maximum ES population. Hydrogen bond analysis does help to rationalise the observed increase in functionality at higher experiment temperatures, however, in agreement with previous observations.[37]

The reaction cavity concept goes some way to explaining the trends in ES population level, particularly when cavity volumes are considered across the structure as a whole. However, analysis of the reaction cavities for individual nitrite sites did not show convincing trends, likely reflecting the fact that, for structures containing multiple photoactive ligands, the switching process is not independent at each site. This point is reinforced by the results of photocrystallographic kinetic analysis, which show that the independent nitrite ligand sites in the same crystal structure isomerise at very similar rates.

In summary, the results of this study reinforce our belief that the nitro → nitrito isomerism process is governed by a complex balance of steric, electronic and kinetic factors and that it is difficult to deconvolute each of these influences. Our ability to uncover convincing trends between structural parameters and the ES populations at each nitrite site is also limited by the fact that steady-state photocrystallographic analysis can only provide static crystal structures of the GS and photostationary ES states and gives no insight into the dynamic structure changes that occur in real time, as individual isomerisation events take place. Time-resolved diffraction studies with materials like **1** would provide vital information and are the subject of future investigation.

Author contributions

L. E. H. was responsible for the conceptualization, funding acquisition and administration of the research programme that produced this work, for the synthesis and photocrystallographic study of **1** and for the formal analysis of all XRD and DFT data. B. A. C. was responsible for collection, data curation and formal analysis of all other analytical data. All authors were involved in writing, reviewing and editing the draft and final manuscript.

Conflicts of interest

There are no conflicts to declare.

Acknowledgements

L. E. H. and B. A. C. are grateful for to the Royal Society for support (URF\R1\191104). In performing DFT calculations we acknowledge the support of the Supercomputing Wales project, which is part-funded by the European Regional Development Fund (ERDF) *via* Welsh Government. We also thank Dr Timothy Easun at Cardiff University for the use of the OceanOptics Flame miniature spectrometer to collect diffuse reflectance spectra.

Notes and references

1 R. Klajn, *Chem. Soc. Rev.*, 2014, **43**, 148–184.
2 S. Crespi, N. A. Simeth and B. König, *Nat. Rev. Chem.*, 2019, **3**, 133–146.

3 S. L. Gilat, S. H. Kawai and J.-M. Lehn, *Chem. – Eur. J.*, 1995, **1**, 275–284.
4 P. Zeng, Z. Liu, Z. Hu, J. Zhai and L. Jiang, *RSC Adv.*, 2013, **3**, 22853–22856.
5 S. D. Stranks and H. J. Snaith, *Nat. Nanotechnol.*, 2015, **10**, 391–402.
6 X. Wu, *et al.*, *Sci. Adv.*, 2017, **3**, e1602388.
7 L. E. Hatcher, J. M. Skelton, M. R. Warren and P. R. Raithby, *Acc. Chem. Res.*, 2019, **52**, 1079–1088.
8 J.-F. Letard, *J. Mater. Chem.*, 2006, **16**, 2550–2559.
9 I. I. Vorontsov, T. Graber, A. Y. Kovalevsky, I. V. Novozhilova, M. Gembicky, Y.-S. Chen and P. Coppens, *J. Am. Chem. Soc.*, 2009, **131**, 6566–6573.
10 K. Kalyanasundaram, *Coord. Chem. Rev.*, 1982, **46**, 159–244.
11 J. M. Cole, K. Y. M. Yeung, G. Pace, S. O. Sylvester, D. Mersch and R. H. Friend, *CrystEngComm*, 2015, **17**, 5026–5031.
12 H. Tsai, R. Asadpour, J.-C. Blancon, C. C. Stoumpos, O. Durand, J. W. Strzalka, B. Chen, R. Verduzco, P. M. Ajayan, S. Tretiak, J. Even, M. A. Alam, M. G. Kanatzidis, W. Nie and A. D. Mohite, *Science*, 2018, **360**, 67.
13 M. Goulkov, D. Schaniel and T. Woike, *J. Opt. Soc. Am. B*, 2010, **27**, 927–932.
14 L. Zeng, X. Guo, C. He and C. Duan, *ACS Catal.*, 2016, **6**, 7935–7947.
15 S.-P. Luo, E. Mejia, A. Friedrich, A. Pazidis, H. Junge, A.-E. Surkus, R. Jackstell, S. Denurra, S. Gladiali, S. Lochbrunner and M. Beller, *Angew. Chem., Int. Ed.*, 2013, **52**, 419–423.
16 A. Maldotti, *Photochemistry*, 2011, **39**, 88–111.
17 N. Alarcos, B. Cohen, M. Ziółek and A. Douhal, *Chem. Rev.*, 2017, **117**, 13639–13720.
18 T. L. Easun, J. Jia, J. A. Calladine, D. L. Blackmore, C. S. Stapleton, K. Q. Vuong, N. R. Champness and M. W. George, *Inorg. Chem.*, 2014, **53**, 2606–2612.
19 D. Hermann, H. Emerich, R. Lepski, D. Schaniel and U. Ruschewitz, *Inorg. Chem.*, 2013, **52**, 2744–2749.
20 J. W. Brown, B. L. Henderson, M. D. Kiesz, A. C. Whalley, W. Morris, S. Grunder, H. Deng, H. Furukawa, J. I. Zink, J. F. Stoddart and O. M. Yaghi, *Chem. Sci.*, 2013, **4**, 2858–2864.
21 S. L. Zheng, M. Messerschmidt and P. Coppens, *Acta Crystallogr., Sect. B: Struct. Sci.*, 2007, **63**, 644–649.
22 S. L. Zheng, M. Gembicky, M. Messerschmidt, P. M. Dominiak and P. Coppens, *Inorg. Chem.*, 2006, **45**, 9281–9289.
23 D. Samanta, J. Gemen, Z. Chu, Y. Diskin-Posner, L. J. W. Shimon and R. Klajn, *Proc. Natl. Acad. Sci. U. S. A.*, 2018, **115**, 9379–9384.
24 A. B. Grommet, L. M. Lee and R. Klajn, *Acc. Chem. Res.*, 2020, **53**, 2600–2610.
25 M. D. Cohen, *Angew. Chem., Int. Ed. Engl.*, 1975, **14**, 386–393.
26 Y. Ohashi, *Crystallogr. Rev.*, 2013, **19**, 2–146.
27 Y. Ohashi, *Acc. Chem. Res.*, 1988, **21**, 268–274.
28 L. E. Hatcher and P. R. Raithby, *Acta Crystallogr., Sect. C: Cryst. Struct. Commun.*, 2013, **69**, 1448–1456.
29 L. E. Hatcher, J. M. Skelton, M. R. Warren, C. Stubbs, E. L. da Silva and P. R. Raithby, *Phys. Chem. Chem. Phys.*, 2018, **20**, 5874–5886.
30 P. Coppens, I. Novozhilova and A. Kovalevsky, *Chem. Rev.*, 2002, **102**, 861–884.
31 M. D. Carducci, M. R. Pressprich and P. Coppens, *J. Am. Chem. Soc.*, 1997, **119**, 2669–2678.
32 A. Y. Kovalevsky, K. A. Bagley and P. Coppens, *J. Am. Chem. Soc.*, 2002, **124**, 9241–9248.
33 K. F. Bowes, J. M. Cole, S. L. G. Husheer, P. R. Raithby, T. L. Savarese, H. A. Sparkes, S. J. Teat and J. E. Warren, *Chem. Commun.*, 2006, 2448–2450.
34 D. V. Fomitchev, K. A. Bagley and P. Coppens, *J. Am. Chem. Soc.*, 2000, **122**, 532–533.
35 M. Warren, S. Brayshaw, A. Johnson, S. Schiffers, P. Raithby, T. Easun, M. George, J. Warren and S. Teat, *Angew. Chem.*, 2009, **121**, 5821–5824.
36 L. E. Hatcher, M. R. Warren, D. R. Allan, S. K. Brayshaw, A. L. Johnson, S. Fuertes, S. Schiffers, A. J. Stevenson, S. J. Teat, C. H. Woodall and P. R. Raithby, *Angew. Chem., Int. Ed.*, 2011, **50**, 8371–8374.
37 L. E. Hatcher and P. R. Raithby, *CrystEngComm*, 2017, **19**, 6297–6304.
38 L. E. Hatcher, *CrystEngComm*, 2016, **18**, 4180–4187.
39 L. E. Hatcher, J. Christensen, M. L. Hamilton, J. Trincao, D. R. Allan, M. R. Warren, I. P. Clarke, M. Towrie, D. S. Fuertes, C. C. Wilson, C. H. Woodall and P. R. Raithby, *Chem. – Eur. J.*, 2014, **20**, 3128–3134.
40 A. E. Phillips, J. M. Cole, T. d'Almeida and K. S. Low, *Phys. Rev. B*, 2010, **82**, 155118.
41 B. Cormary, S. Ladeira, K. Jacob, P. G. Lacroix, T. Woike, D. Schaniel and I. Malfant, *Inorg. Chem.*, 2012, **51**, 7492–7501.
42 M. R. Warren, T. L. Easun, S. K. Brayshaw, R. J. Deeth, M. W. George, A. L. Johnson, S. Schiffers, S. J. Teat, A. J. Warren, J. E. Warren, C. C. Wilson, C. H. Woodall and P. R. Raithby, *Chem. – Eur. J.*, 2014, **20**, 5468–5477.
43 L. E. Hatcher, *CrystEngComm*, 2018, **20**, 5990–5997.
44 D. Schaniel and T. Woike, *Phys. Chem. Chem. Phys.*, 2009, **11**, 4391–4395.
45 L. E. Hatcher, E. J. Bigos, M. J. Bryant, E. M. MacCready, T. P. Robinson, L. K. Saunders, L. H. Thomas, C. M. Beavers, S. J. Teat, J. Christensen and P. R. Raithby, *CrystEngComm*, 2014, **16**, 8263–8271.
46 A. Makal, J. Benedict, E. Trzop, J. Sokolow, B. Fournier, Y. Chen, J. A. Kalinowski, T. Graber, R. Henning and P. Coppens, *J. Phys. Chem. A*, 2012, **116**, 3359–3365.
47 S. A. Labb, C. J. Masteran, S. G. Albright, B. Ali, H. A. Chapman, Y. Cheng, R. M. Cusic, N. B. Hartlove, A. N. Marr, M. Timmons and S. J. Friese, *Synlett*, 2020, **31**, 1384–1388.
48 CrysAlisPro data collection and data reduction GUI, Rigaku, version 171.40.67a (2021).
49 G. Sheldrick, *Acta Crystallogr., Sect. A: Found. Adv.*, 2015, **71**, 3–8.
50 G. Sheldrick, *Acta Crystallogr., Sect. C: Struct. Chem.*, 2015, **71**, 3–8.
51 S. K. Brayshaw, J. W. Knight, P. R. Raithby, T. L. Savarese, S. Schiffers, S. J. Teat, J. E. Warren and M. R. Warren, *J. Appl. Crystallogr.*, 2010, **43**, 337–340.

52 M. P. Fuller and P. R. Griffiths, *Anal. Chem.*, 1978, **50**, 1906–1910.
53 C. Lee, W. Yang and R. G. Parr, *Phys. Rev. B*, 1988, **37**, 785–789.
54 A. D. Becke, *J. Chem. Phys.*, 1993, **98**, 5648–5652.
55 M. J. Frisch, G. W. Trucks, H. B. Schlegel, G. E. Scuseria, M. A. Robb, J. R. Cheeseman, G. Scalmani, V. Barone, B. Mennucci, G. A. Petersson, H. Nakatsuji, M. Caricato, X. Li, H. P. Hratchian, A. F. Izmaylov, J. Bloino, G. Zheng, J. L. Sonnenberg, M. Hada, M. Ehara, K. Toyota, R. Fukuda, J. Hasegawa, M. Ishida, T. Nakajima, Y. Honda, O. Kitao, H. Nakai, T. Vreven, J. A. Montgomery, Jr., J. E. Peralta, F. Ogliaro, M. Bearpark, J. J. Heyd, E. Brothers, K. N. Kudin, V. N. Staroverov, R. Kobayashi, J. Normand, K. Raghavachari, A. Rendell, J. C. Burant, S. S. Iyengar, J. Tomasi, M. Cossi, N. Rega, J. M. Millam, M. Klene, J. E. Knox, J. B. Cross, V. Bakken, C. Adamo, J. Jaramillo, R. Gomperts, R. E. Stratmann, O. Yazyev, A. J. Austin, R. Cammi, C. Pomelli, J. W. Ochterski, R. L. Martin, K. Morokuma, V. G. Zakrzewski, G. A. Voth, P. Salvador, J. J. Dannenberg, S. Dapprich, A. D. Daniels, Ö. Farkas, J. B. Foresman, J. V. Ortiz, J. Cioslowski and D. J. Fox, *GAUSSIAN 09 (Revision A.1)*, Gaussian Inc., Wallingford CT, 2009.
56 M. D. Hanwell, D. E. Curtis, D. C. Lonie, T. Vandermeersch, E. Zurek and G. R. Hutchison, *J. Cheminf.*, 2012, **4**, 17.
57 Creating UV/Visible Plots from the Results of Excited States Calculations, Gaussian Inc., viewed 27 September 2021, <**https://gaussian.com/uvvisplot/**>.
58 J. J. McKinnon, F. P. A. Fabbiani and M. A. Spackman, *Cryst. Growth Des.*, 2007, **7**, 755–769.
59 M. A. Spackman and J. J. McKinnon, *CrystEngComm*, 2002, **4**, 378–392.
60 C. F. Macrae, I. Sovago, S. J. Cottrell, P. T. A. Galek, P. McCabe, E. Pidcock, M. Platings, G. P. Shields, J. S. Stevens, M. Towler and P. A. Wood, *J. Appl. Crystallogr.*, 2020, **53**, 226–235.
61 A. A. Mikhailov, V. Y. Komarov, A. S. Sukhikh, D. P. Pishchur, D. Schaniel and G. A. Kostin, *New J. Chem.*, 2020, **44**, 18014–18024.
62 I. Abdelmoty, V. Buchholz, L. Di, C. Guo, K. Kowitz, V. Enkelmann, G. Wegner and B. M. Foxman, *Cryst. Growth Des.*, 2005, **5**, 2210–2217.
63 V. Enkelmann, G. Wegner, K. Novak and K. B. Wagener, *J. Am. Chem. Soc.*, 1993, **115**, 10390–10391.
64 S. E. Bajwa, T. E. Storr, L. E. Hatcher, T. J. Williams, C. G. Baumann, A. C. Whitwood, D. R. Allan, S. J. Teat, P. R. Raithby and I. J. S. Fairlamb, *Chem. Sci.*, 2012, **3**, 1656–1661.
65 M. Avrami, *J. Chem. Phys.*, 1939, **7**, 1103–1112.
66 M. Avrami, *J. Chem. Phys.*, 1940, **8**, 212–224.
67 M. Avrami, *J. Chem. Phys.*, 1941, **9**, 177–184.
68 G. A. Jeffrey, *An Introduction to Hydrogen Bonding*, Oxford University Press, 1997.
69 M. D. Cohen and G. M. J. Schmidt, *J. Chem. Soc.*, 1964, 1996–2000.
70 M. D. Cohen, G. M. J. Schmidt and F. I. Sonntag, *J. Chem. Soc.*, 1964, 2000–2013.
71 M. R. Warren, S. K. Brayshaw, L. E. Hatcher, A. L. Johnson, S. Schiffers, A. J. Warren, S. J. Teat, J. E. Warren, C. H. Woodall and P. R. Raithby, *Dalton Trans.*, 2012, **41**, 13173–13179.
72 P. Coppens, J. Sokolow, E. Trzop, A. Makal and Y. Chen, *J. Phys. Chem. Lett.*, 2013, 579–582, DOI: **10.1021/jz400013b**.

